

X-ray study of the double source plane gravitational lens system Eye of Horus observed with XMM-Newton

Keigo Tanaka^{1*}, Ayumi Tsuji¹, Hiroki Akamatsu², J. H. H. Chan³, Jean Coupon⁴, Eiichi Egami⁵, Francois Finet⁶, Ryuichi Fujimoto⁷, Yuto Ichinohe⁸, Anton T. Jaelani⁹, Chien-Hsiu Lee⁶, Ikuyuki Mitsuishi¹⁰, Anupreeta More¹¹, Surhud More¹², Masamune Oguri^{12,13,14}, Nobuhiro Okabe¹⁵, Naomi Ota¹⁶, Cristian E. Rusu⁶, Alessandro Sonnenfeld¹², Masayuki Tanaka¹⁷, Shutaro Ueda¹⁸, and Kenneth C. Wong^{12,17}

¹ Graduate School of Natural Science & Technology, Kanazawa University, Kakuma-machi, Kanazawa, Ishikawa 920-1192, Japan

² SRON Netherlands Institute for Space Research, Sorbonnelaan 2, 3584 CA Utrecht, the Netherlands

³ Institute of Physics, Laboratory of Astrophysics, Ecole Polytechnique Fédérale de Lausanne (EPFL), Observatoire de Sauverny, 1290 Versoix, Switzerland

⁴ Department of Astronomy, University of Geneva, ch. d'Écogia 16, 1290 Versoix, Switzerland

⁵ Steward Observatory, University of Arizona, 933 North Cherry Avenue, Tucson, AZ 85721, USA

⁶ Subaru Telescope, NAOJ, 650 N Aohoku Pl, Hilo, HI 96720, USA

⁷ Faculty of Mathematics and Physics, Kanazawa University, Kakuma-machi, Kanazawa, Ishikawa 920-1192, Japan

⁸ Department of Physics, Rikkyo University, Nishi Ikebukuro 3-3-4-1, Toshimaku, Tokyo, Japan

⁹ Department of Physics, Kindai University, Higashi-Osaka, Osaka 577-8502, Japan

¹⁰ Department of Physics, Nagoya University, Furo-cho, Chikusa-ku, Nagoya, Aichi 464-8602, Japan

¹¹ Inter-University Centre for Astronomy and Astrophysics, Post Bag 4, Ganeshkhind, Pune 411 007, India

¹² Kavli IPMU (WPI), UTIAS, The University of Tokyo, Kashiwa, Chiba 277-8583, Japan

¹³ Research Center for the Early Universe, University of Tokyo, 7-3-1 Hongo, Bunkyo-ku, Tokyo 113-0033, Japan

¹⁴ Department of Physics, University of Tokyo, 7-3-1 Hongo, Bunkyo-ku, Tokyo 113-0033, Japan

¹⁵ Department of Physical Science, Hiroshima University, 1-3-1 Kagamiyama, Higashi-Hiroshima, Hiroshima 739-8526, Japan

¹⁶ Department of Physics, Nara Women's University, Kitauoyanishi-machi, Nara, 630-8506, Japan

¹⁷ National Astronomical Observatory of Japan, Mitaka, Tokyo 181-8588, Japan

¹⁸ Academia Sinica Institute of Astronomy and Astrophysics (ASIAA), No. 1, Section 4, Roosevelt Road, Taipei 10617, Taiwan

Accepted XXX. Received YYY; in original form ZZZ

ABSTRACT

A double source plane (DSP) system is a precious probe for the density profile of distant galaxies and cosmological parameters. However, these measurements could be affected by the surrounding environment of the lens galaxy. Thus, it is important to evaluate the cluster-scale mass for detailed mass modeling. We observed the *Eye of Horus*, a DSP system discovered by the Subaru HSC-SSP, with XMM-Newton. We detected two X-ray extended emissions, originating from two clusters, one centered at the *Eye of Horus*, and the other located ~ 100 arcsec northeast to the *Eye of Horus*. We determined the dynamical mass assuming hydrostatic equilibrium, and evaluated their contributions to the lens mass interior of the Einstein radius. The contribution of the former cluster is $1.1^{+1.2}_{-0.5} \times 10^{12} M_{\odot}$, which is 21 – 76% of the total mass within the Einstein radius. The discrepancy is likely due to the complex gravitational structure along the line of sight. On the other hand, the contribution of the latter cluster is only $\sim 2\%$ on the *Eye of Horus*. Therefore, the influence associated with this cluster can be ignored.

Key words: galaxies: clusters: individual: HSC J142449-005322 – gravitational lensing: strong – galaxies: clusters: intracluster medium

* E-mail: tanaka@astro.s.kanazawa-u.ac.jp (Kanazawa Univer-

1 INTRODUCTION

The *Eye of Horus* is a strong gravitational lens object (Tanaka et al. 2016) that was discovered by the Subaru HSC-SSP survey (HSC-SSP; Aihara et al. 2018b,a; Miyazaki et al. 2018; Komiyama et al. 2018; Kawanomoto et al. 2018; Furusawa et al. 2018; Bosch et al. 2018; Huang et al. 2018; Coupon et al. 2018). It is known as a precious double source plane (DSP) object. The lens galaxy of the *Eye of Horus* is a massive (stellar mass $\sim 7 \times 10^{11} M_{\odot}$) early-type galaxy which is located at (RA, DEC)=(14^h24^m49^s.0, -00°53'21"65) (J2000), and the redshift of the lens galaxy is $z = 0.795$. Since there are two background galaxies behind the lens galaxy whose redshifts are $z = 1.302$ and 1.988 , respectively, an Einstein ring and an arc corresponding to these background galaxies are projected near the Einstein radii.

DSP system is a precious probe for the gravitational structure of lens galaxies and cosmological parameters. In a distant galaxy at $z \sim 0.8$, it is usually difficult to determine the gravitational structure inside the galaxy using only the stellar distribution. However, when a lens galaxy has a double source lens image, the gravitational structure at 10–100 kpc can be determined by combining lensing and dynamics, even if it is located at $z \sim 0.8$ (e.g., Sonnenfeld et al. 2012). The matter density parameter Ω_M , the equation of state parameter ω , and the Hubble parameter by cosmic microwave background (CMB) measurements (Komatsu et al. 2011) degenerate. On the other hand, measurements of the ratio of two Einstein radii in a DSP object enables us to break the degeneracy between the Hubble parameter and the other two parameters (Collett et al. 2012; Collett & Auger 2014; Linder 2016).

The above constraints are obtained with high accuracy if the lens galaxy is an isolated system. However, Keeton & Zabludoff (2004) suggested that if it lies in a group or a cluster of galaxies, the lens image would be affected by the environment surrounding the lens galaxy, depending on the distance between lens galaxy and the group/cluster center. The lens galaxy of the *Eye of Horus* corresponds to the brightest cluster galaxy (BCG) of HSC J142449-005322 (hereafter the main cluster) in the CAMIRA cluster catalog (Oguri et al. 2018). The richness of this cluster is $N_{\text{gal}} \sim 34$, and its redshift is $z \sim 0.801$. However, BCGs identified by optical data are known to often deviate from the cluster center up to several hundred kpc (Oguri et al. 2018). Therefore, we should determine the cluster center position accurately using X-ray data. Furthermore, Oguri et al. (2018) suggested that there is another cluster (HSC J142456-005157, hereafter the north-east (NE) cluster) located at (RA, DEC)=(14^h24^m56^s.4, -00°51'57"39) (J2000). The richness is $N_{\text{gal}} \sim 37$, and its redshift is $z \sim 0.768$. These two clusters are separated only by $\sim 2'$, and photometric data suggests that the difference of the redshifts is only $\Delta z \sim 0.03$, so the gravitational potential of the NE cluster may affect the lens image. If these two clusters are a merger, the lens model of the *Eye of Horus* may be complicated.

X-ray observations provide us with crucial information on the cluster-scale environment. We observed X-ray emission surrounding the *Eye of Horus* with *XMM-Newton* and report the results in this paper. Two extended emissions were detected at the position of these two clusters (§2).

We fitted the X-ray image to determine the center position and the extension of the intracluster medium (ICM) of each cluster (§3). We fitted their spectra to determine the temperature of the ICM (§4). We calculated the cluster mass assuming hydrostatic equilibrium (hereafter hydrostatic mass), based on the parameters obtained by image fitting and spectral fitting, and we evaluated the effect of the cluster-scale dynamical mass on the lens potential (§6).

Throughout this paper, we adopt a Hubble constant of $H_0 = 70 \text{ km s}^{-1} \text{ Mpc}^{-1}$, and cosmological density parameters of $\Omega_M = 0.27$ and $\Omega_{\Lambda} = 0.73$. $1''$ corresponds to 7.64 kpc at the main cluster and 7.52 kpc at the NE cluster, respectively. The solar abundance table by Lodders & Palme (2009) is used. All error ranges are 68% confidence intervals unless otherwise stated.

2 OBSERVATION AND DATA REDUCTION

The *Eye of Horus* was observed with *XMM-Newton* on 2018 January 6. Table 1 shows detail information on the observation. The medium filter for MOS (Turner et al. 2001) and the thin filter for pn (Strüder et al. 2001) were selected, respectively. We used SAS version 17.0.0 to extract images and spectra, and CCF version XMM-CCF-REL-356 as a calibration database. We used the data analysis pipeline of Miyaoka et al. (2018) to adopt the standard data reduction. Raw data were filtered with the standard method and the events that matched the conditions of FLAG = 0 and PATTERN ≤ 12 for MOS, and FLAG = 0 and PATTERN ≤ 4 for pn were extracted. Bright point sources were excluded by using `cheese` command.

Fig. 1 shows a composite image of MOS1, 2 and pn in the 0.4–2.3 keV band. In addition to the main cluster and the NE cluster, a couple of sources were detected. There are two very bright point sources, $\sim 1'$ and $\sim 2'$ northwest of the main cluster (hereafter NW PS and far NW PS). There are two faint point sources, $\sim 30''$ east of the main cluster and $\sim 1'$ south-southeast of the NE cluster, respectively (hereafter the 2nd-peak and the 3rd-peak).

3 IMAGING ANALYSIS

We fitted the X-ray image to determine the center coordinates of the main cluster and the NE cluster. A fitting area of $315''$ square, roughly centered at the main cluster, was selected to evaluate background properly as shown in Fig. 1. The NW PS and the far NW PS are brighter than the main cluster, so the circular regions with a radius of $30''$ centered at the point sources were excluded.

We used Sherpa (Freeman et al. 2001) in CIAO version 4.10 (Fruscione et al. 2006) for image fitting. The source distribution models were convolved with the PSF model and the exposure maps. The PSF maps were generated at the energy of 1.35 keV and at the on-axis position using `psfgen` tool. The images, the PSF maps, and the exposure maps were rebinned so that the pixel size becomes $5''$. The three images were fitted simultaneously using the C statistic (Cash 1979).

We adopted a 2-dimensional single- β model for the main cluster, a 2-dimensional double- β model for the NE cluster,

Table 1. Observation log. The flare time is removed from the exposure time.

Target name	Obs ID	Start time [UT]	Exposure time (MOS1 / MOS2 / pn) [ks]	RA	Dec
HSC J142449-0053	0800790101	2018-01-06 06:26:13	43.4 / 44.5 / 30.0	14:24:49.0	-00:53:21.6

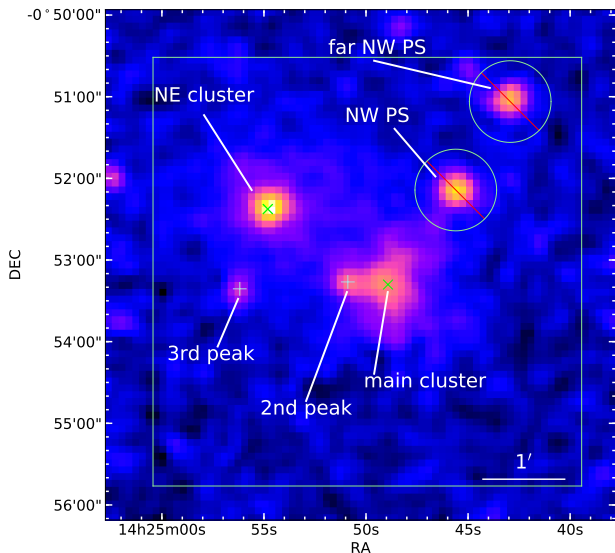


Figure 1. X-ray surface brightness distribution near the *Eye of Horus*. It is a merged image of MOS1, 2 and pn in the 0.4–2.3 keV band, after subtracting the non-X-ray background (NXB), correcting exposure-time, and smoothing with $\sigma = 5''$. The green lines show the region for image fitting. The green and the blue cross points show the best-fit center positions of each source obtained from image fitting.

a 2-dimensional delta function for the 2nd-peak and the 3rd-peak, respectively, and a constant for the background component. We set the central coordinates of each source model as free parameters. The parameters of the corresponding models were linked with each other among the detectors, except for the normalizations. Two β 's of the double- β model used for the NE cluster were also linked. The normalizations of the corresponding models were constrained so that the ratio becomes the same among the detectors.

Table 2 shows the result of the image fitting. The center coordinates of each cluster were obtained with an accuracy of $\sim 1''$ and each parameter was converged to an appropriate value as a cluster. Note that, when we removed the constraints of the normalizations, β of the NE cluster became relatively small ($\beta = 0.46^{+0.10}_{-0.02}$) compared with typical clusters ($\beta = 0.64 \pm 0.32$, Ota & Mitsuda 2004). Also note that β became inappropriate when we unlinked the two β of the double β -model or change the double β -model to the single β -model at the NE cluster.

Fig. 2 shows an X-ray contour map superposed on the optical image. The positions of the X-ray sources are denoted by the green crosses. The X-ray peak of the main cluster is consistent with the optical position of the *Eye of Horus*. It is also consistent with the result of CAMIRA cluster finding algorithm that HSC J142449-005322 is the central galaxy of

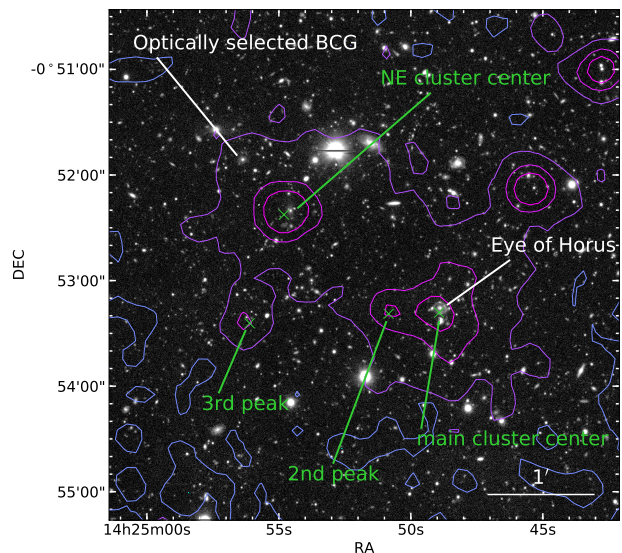


Figure 2. X-ray contours generated from Fig. 1, superposed on the optical image observed with Subaru–HSC. Green crosses show the best-fit center positions of the main cluster, the NE cluster, the 2nd peak, and the 3rd peak.

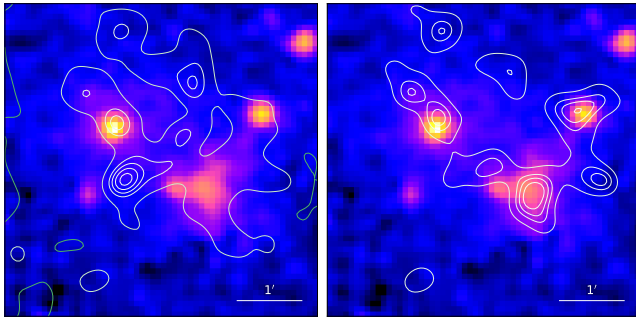
the main cluster. But the center position determined from image fit is $3.8 \pm 1.0''$ shifted to the south from the center of the *Eye of Horus*. On the other hand, the best-fit position of the NE cluster deviated considerably ($\sim 40''$) from the optically selected BCG (see Fig. 2), which is probably due to an error of optical identification, since CAMIRA cluster finding algorithm has a certain uncertainty in the determination of the BCG. There is an elliptical galaxy SDSS J142454.68-005226.3, $3.8 \pm 0.5''$ northwest of the X-ray peak of the NE cluster, and we infer that this object is the correct BCG of the NE cluster. The X-ray peak of the main cluster and the NE cluster shifted $3.8 \pm 1.0''$ south and $3.8 \pm 0.5''$ southeast from the optical counterpart, respectively. These discrepancies are higher than the position uncertainty of the EPIC, which is $1.2''$ (1σ) according to XMM-Newton Calibration Technical Notes v3.11¹, and we infer that these discrepancies are caused by the cluster-scale structure.

We investigated whether the main cluster and the NE cluster are a merger. Fig. 3 shows a contour map of the galaxy probability density distribution in the redshift band of each cluster generated by MIZUKI (Tanaka 2015), overlaid with the X-ray image. MIZUKI determines the probability density distribution of the galaxies at any redshift from the photometric data. From the left panel, in the redshift band of the NE cluster, the galaxy density is relatively

¹ <http://xmm2.esac.esa.int/docs/documents/CAL-TN-0018.pdf>

Table 2. Best-fit parameters obtained from the image fitting.

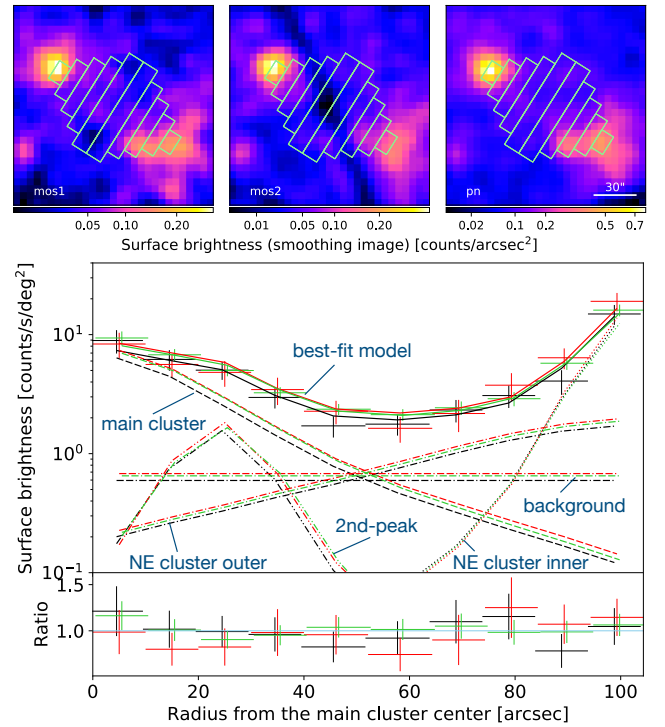
Parameter	Main cluster	NE cluster inner	NE cluster outer	2nd-peak	3rd-peak	Background
r_c [arcsec / kpc]	$21.5^{+4.1}_{-1.9} / 194^{+31}_{-15}$	$2.27^{+0.62}_{-0.16} / 17.1^{+4.7}_{-1.2}$	$60.0^{+9.7}_{-5.6} / 451^{+73}_{-42}$	-	-	-
β	$0.67^{+0.08}_{-0.03}$		$0.78^{+0.14}_{-0.06}$	-	-	-
RA [deg]	$216.20386^{+0.00030}_{-0.00029}$		$216.22837^{+0.00012}_{-0.00011}$	$216.21185^{+0.00108}_{-0.00031}$	$216.23378^{+0.00136}_{-0.00002}$	-
DEC [deg]	$-0.89034^{+0.00027}_{-0.00029}$		$-0.87489^{+0.00014}_{-0.00016}$	$-0.89053^{+0.00077}_{-0.00061}$	$-0.89204^{+0.00089}_{-0.00050}$	-
norm _{MOS1} [cnt/s/deg ²]	$11.6^{+0.7}_{-0.4}$	518^{+466}_{-167}	2.0 ± 0.3	82 ± 16	59 ± 10	0.60 ± 0.03
norm _{MOS2} [cnt/s/deg ²]	$13.3^{+1.0}_{-0.9}$	= norm(MOS2, main cluster) \times norm(MOS1, each component) / norm(MOS1, main cluster)				
norm _{pn} [cnt/s/deg ²]	$12.7^{+0.8}_{-0.5}$	= norm(pn, main cluster) \times norm(MOS1, each component) / norm(MOS1, main cluster)				
C-statistic				16011		
d.o.f.				11208		
C-statistic/d.o.f.				1.429		

**Figure 3.** Galaxy probability density distribution contours at $0.762 < z < 0.774$ (left) and $0.795 < z < 0.807$ (right), overlaid with the X-ray image. The redshifts correspond to the NE cluster and the main cluster, respectively. The X-ray image is the same as Fig. 1

low around the main cluster, and there are some peaks of the galaxy density around the NE cluster. However, from the right panel, these peaks around the NE cluster also exist in the redshift band of the main cluster. Therefore, it is not clear from photometric data whether these two clusters are a merger or not. Fig. 4 shows the X-ray surface brightness profile between the main cluster and the NE cluster. When the two clusters are a merger, it is known that excess of X-ray emission is observed between two clusters, due to compression of ICM by the merging (e.g., between A399 and A401, Fujita et al. 1996). However, there is no significant excess emission beyond the error range over the sum of the two cluster models between the main cluster and the NE cluster. This result indicates that these two clusters are likely not a merger.

4 SPECTRAL ANALYSIS

We fitted the EPIC spectra to determine the ICM temperatures of the two clusters. Fig. 5 shows the definition of the spectral integration regions. From the imaging analysis, we found that the intensity of cluster emission reaches the background level at the radius of $\sim 100''$ (764 and 752 kpc for

**Figure 4.** The X-ray surface brightness profile between the main cluster and the NE cluster (black: MOS1, red: MOS2, green: pn). The top panels show extracted regions of X-ray surface brightness. The dashed, dotted, dash-dotted, dot-dot-dashed, dash-dash-dotted lines correspond to the main cluster, the NE cluster outer, the NE cluster inner, the 2nd-peak, the background components of the best-fit model, respectively, and the solid line shows the sum of them.

the main and the NE cluster, respectively). Therefore, with a margin, let the radius $2'$ be the boundary between each cluster region and the background region. Since the main cluster and the NE cluster are separated only by $\sim 100''$, we divided the regions of the main cluster and the NE cluster at the midpoint between them. The background region was defined as a circle of a radius of $8'$ centered at the midpoint,

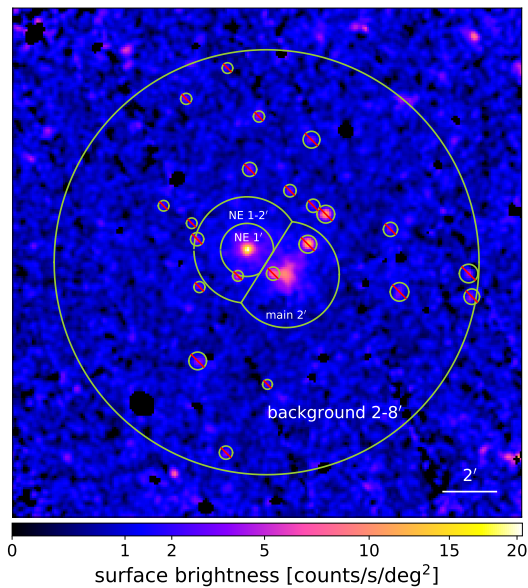


Figure 5. Source and background regions for spectral fitting. The image is the same as Fig. 1

Table 3. Photon counts in the four regions. The energy bands are 0.3–11 keV for the MOS spectra and 0.4–11 keV for the pn spectra, respectively. The net count means the QPB-subtracted count.

Region	Instrument	Counts	Net counts
Main cluster	MOS1	1683	1129.1
	MOS2	1678	1115.3
	pn	3560	2022.9
NE cluster inner	MOS1	685	571.3
	MOS2	725	577.7
	pn	1692	1297.3
NE cluster outer	MOS1	932	490.5
	MOS2	804	494.1
	pn	1183	815.4
Background	MOS1	17059	7703.5
	MOS2	21771	8985.0
	pn	41210	19698.7

excluding the main cluster and the NE cluster regions. Note that, the NE cluster region was divided into the inner region ($r \leq 1'$) and the outer region ($1' < r \leq 2'$) to consider temperature gradient because the X-ray emission of the NE cluster is concentrated in the central region. There are many point sources in these regions. Bright point sources were removed by the `cheese` command. Faint point sources that can be distinguished by eye, but cannot be removed by `cheese` command were manually removed. Table 3 summarizes photon counts of the four regions.

Quiescent particle background (QPB) spectra were generated using `mos_back` and `pn_back` and subtracted from the spectra of the four regions. Then the spectra were rebinned

Table 4. Results of the spectral fitting of the cluster regions.

parameter	Main cluster	NE cluster inner	NE cluster outer
kT [keV]	$6.07^{+1.22}_{-0.89}$	$3.30^{+0.47}_{-0.40}$	$0.94^{+0.87}_{-0.32}$
Abundance [Z_{\odot}]	$0.21^{+0.35}_{-0.21}$		$0.06^{+0.25}_{-0.06}$
Redshift	0.80094 (fixed)		0.76828 (fixed)
d.o.f.		1284	
χ^2		1625.04	
Reduced- χ^2		1.266	

so that each bin contained at least 20 counts. The energy band was set to 0.3–11.0 keV for MOS and 0.4–11.0 keV for pn.

We used XSPEC version 12.10.1 (Arnaud 1996) for spectral fitting. We adopted the APEC version 3.0.9 (Smith et al. 2001) as an optically thin thermal plasma model. We adopted `phabs` as a photoelectric absorption model, and the column density was fixed at $3.25 \times 10^{20} \text{ cm}^{-2}$ based on the LAB survey (Kalberla et al. 2005). EPIC spectra have many background components (De Luca & Molendi 2004; Kuntz & Snowden 2008; Freyberg et al. 2004; Snowden et al. 2004; Carter & Sembay 2008). We fitted all the spectra of the detectors and the four regions simultaneously following Snowden et al. (2008).

Emission of each cluster was represented by `phabs*apec`, and the parameters were linked among detectors. The redshift of each cluster was fixed at the value derived from photometric data (Oguri et al. 2018). The abundances of the NE cluster component in the inner and the outer regions were linked with each other. The projection effects are considered, assuming that each source is spherically symmetric with constant density.

The response files were created by SAS tools. RMFs were generated together with spectra using `mos-spectra` and `pn-spectra` tools. We adopted extended source ARFs that were generated using `arfgen` tool. We adopted χ^2 statistic to the statistical test.

Fig. 6 and Table 4 show the best-fit parameters of the spectral fitting. From Table 4, the temperature of the NE cluster has radial dependence although it is marginal. We also tested whether there is a temperature gradient in the main cluster, by dividing the region of the main cluster into two, an inner circle of $1'$ radius and an annulus of $2'$ outer radius, but we could not find the difference in the temperature between the two regions ($kT_{\text{in}} = 5.6^{+0.8}_{-0.7}$ keV, $kT_{\text{out}} = 5.9^{+14}_{-2.8}$ keV). When the redshifts were made free, they became unacceptably high ($z_{\text{main}} = 2.71^{+0.13}_{-0.08}$, $z_{\text{NE}} = 3.71^{+0.24}_{-0.12}$). Note that, since the instrumental Al $K\alpha$ and Si $K\alpha$ lines are predominant in the 1.3–1.9 keV range in MOS spectra and in the 1.3–1.6 keV range in pn spectra (see Fig 6), we evaluated the influence of these lines to the fitting result by excluding these energy ranges. The parameters of the ICM unchanged within the error ranges of Table 4.

From the result of image fitting and spectral fitting, the surface brightness distribution of the NE cluster is well represented by a double- β model, and the spectrum is represented by a two-temperature model. These results suggest

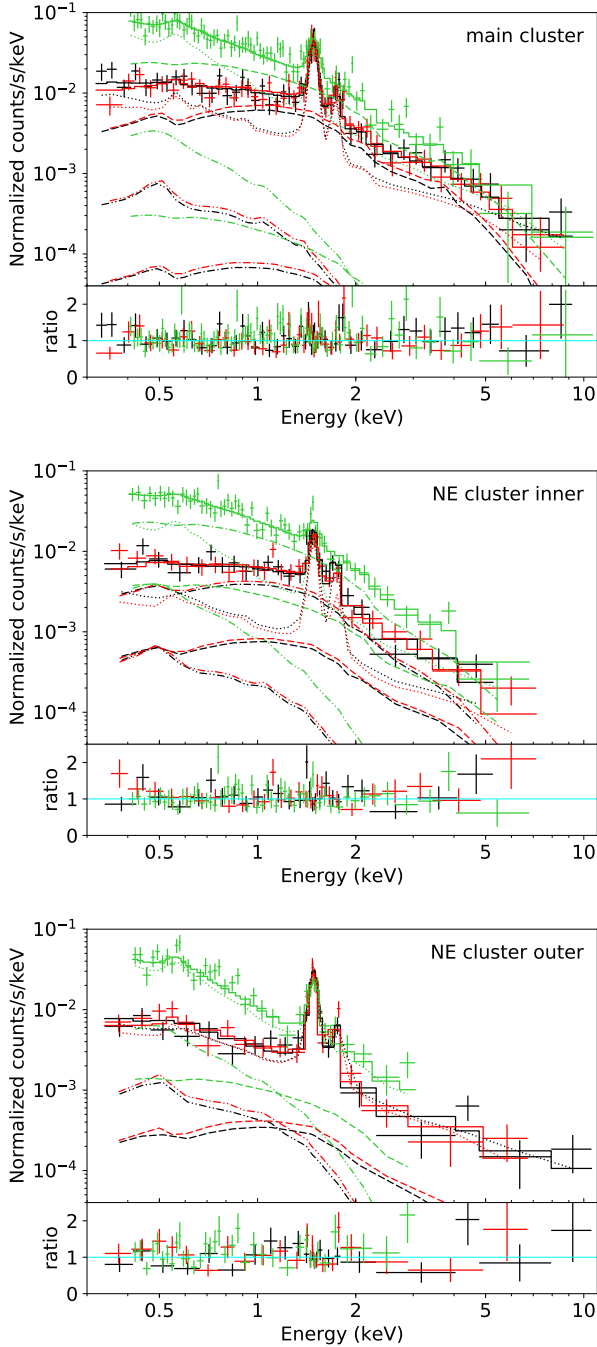


Figure 6. QPB-subtracted spectra and best-fit models of the three source regions (black: MOS1, red: MOS2, green: pn). The dashed, dot-dashed, dot-dot-dashed and dotted lines show the main cluster, the NE cluster inner, the NE cluster outer and the background component, respectively.

that the NE cluster is divided into two components, the inner component ($r_c = 2.44^{+0.60}_{-0.16}$ arcsec, $kT = 3.30^{+0.47}_{-0.40}$ keV) and outer component ($r_c = 57.8^{+9.1}_{-5.5}$ arcsec, $kT = 0.94^{+0.87}_{-0.32}$ keV), and the gravitational potential of the NE cluster is concentrated in the central elliptical galaxy.

5 DISCUSSION

5.1 Mass of the clusters

Based on the distributions and the temperatures of the ICM obtained by the results of the image fitting and the spectral fitting, we calculated the hydrostatic mass of the main cluster and the NE cluster, and evaluated the effect of the cluster-scale environment on the lens image of the *Eye of Horus*. When the ICM is in hydrostatic equilibrium and its surface brightness distribution follows a β -model, the hydrostatic mass density at a radius r from the cluster center can be represented as follows (Ota et al. 1998)

$$\rho(r) = \frac{1}{4\pi r^2} \cdot \frac{3k_B T \beta}{G \bar{m}} \left\{ \frac{3r^2}{r^2 + r_c^2} - \frac{2r^4}{(r^2 + r_c^2)^2} \right\}, \quad (1)$$

where k_B , \bar{m} , and G are the Boltzmann constant, the average ion mass, and the gravitational constant, respectively. From this equation, the hydrostatic mass which are projected on the sky plane within a radius r is given by

$$M(r) = \frac{3k_B T \beta r}{G \bar{m}} \cdot \frac{r^2}{r^2 + r_c^2}. \quad (2)$$

r_{200} (r_{500}) is defined as the radius within which the average density is 200 (500) times the critical density, and M_{200} (M_{500}) is the hydrostatic mass within r_{200} (r_{500}), i.e.,

$$M_{200} \equiv M(r_{200}) = 200 \cdot \frac{3H^2}{8\pi G} \cdot \frac{4\pi}{3} \cdot r_{200}^3, \quad (3)$$

and

$$M_{500} \equiv M(r_{500}) = 500 \cdot \frac{3H^2}{8\pi G} \cdot \frac{4\pi}{3} \cdot r_{500}^3, \quad (4)$$

where H is the Hubble parameter, $H = 106 \text{ km s}^{-1} \text{ Mpc}^{-1}$ for the main cluster and $H = 104 \text{ km s}^{-1} \text{ Mpc}^{-1}$ for the NE cluster, respectively. Using equations (2) and (3) or (4), r_{200} and M_{200} , or r_{500} and M_{500} , can be determined. Since the NE cluster has two components, when we use equation (2) for the NE cluster, we combined the inner component and the outer component with their density ratio.

Table 5 shows M_{200} , M_{500} and r_{200} , r_{500} thus obtained. We confirmed that there are two massive cluster, $5.6^{+1.3}_{-0.8} \times 10^{14} M_\odot$ and $2.2^{+0.5}_{-0.3} \times 10^{14} M_\odot$, respectively, in the field of the *Eye of Horus*. The cluster mass inferred from the mass-richness scaling relation (Okabe et al. 2018) is also shown in Table 6 for comparison. The two clusters have comparable optical mass, while the hydrostatic mass of the main cluster estimated by the X-ray data is almost three times larger than that obtained from the mass-richness relation. This is probably because measurement of the number of the member galaxies has large uncertainty in the distant cluster, and we assumed spherical symmetry and extrapolated the isothermal single- β model to the outside where X-ray emission cannot be seen.

5.2 Mass within the Einstein radius

The total mass M_{tot} projected on the sky plane within the Einstein radius can be calculated from the Einstein radius of the lens galaxy, and angular diameter distances to the lens galaxy, to the background source, and between the lens

Table 5. M_{200} and M_{500} of the main cluster and the NE cluster determined by the X-ray data.

source	Main cluster	NE cluster
r_{200} (arcsec / Mpc)	168 / 1.28	127 / 0.95
r_{500} (arcsec / Mpc)	105 / 0.80	80 / 0.60
M_{200} (M_{\odot})	$5.6^{+1.3}_{-0.8} \times 10^{14}$	$2.2^{+0.5}_{-0.3} \times 10^{14}$
M_{500} (M_{\odot})	$3.4^{+0.8}_{-0.5} \times 10^{14}$	$1.4^{+0.3}_{-0.2} \times 10^{14}$

Table 6. M_{200} and M_{500} of the main cluster and the NE cluster inferred from the mass-richness scaling.

source	Main cluster	NE cluster
N_{gal}	34	37
M_{200} (M_{\odot})	2.2×10^{14}	2.5×10^{14}
M_{500} (M_{\odot})	1.4×10^{14}	1.6×10^{14}

galaxy and the background source. The *Eye of Horus* has two background galaxies (S1 and S2 in Tanaka et al. 2016) and Einstein radii. The Einstein radius of S2 is affected not only by the lens galaxy but also by S1 since S2 is located behind S1. Therefore, in this paper, we only used S1. Since the Einstein radius of the S1 is 2.14 ± 0.02 arcsec (Sonnenfeld et al. 2019), M_{tot} is $(2.98 \pm 0.04) \times 10^{12} M_{\odot}$, which is ~ 4.5 times the stellar mass of the lens galaxy ($6.6^{+0.7}_{-0.1} \times 10^{11} M_{\odot}$, Tanaka et al. 2016).

Using equation (1), we calculated M_E , the mass of each cluster projected on the sky plane within the Einstein radius of the lens galaxy, which is summarized in Table 7. In calculating M_E for each cluster, we extrapolated the result of the image and spectral fitting to a sufficiently distant point along the line of sight where the mass calculation converges, although the X-ray emission can be seen only up to $\sim r_{500}$. Note that, we considered a statistical error ($1.0''$) and XMM position uncertainty ($1.2''$) as a position error.

M_E of the main cluster is $1.1^{+0.7}_{-0.4} \times 10^{12} M_{\odot}$, which is larger than the stellar mass of the lens galaxy, yet explains only 25 – 60% of M_{tot} . Therefore, we investigated the cause of the discrepancy. First, we tested an NFW density profile (Navarro et al. 1996) for the mass estimation because it has steeper and deeper potential at the central region than that of a single- β model. We used relation between the scale radius of the NFW density profile r_s and the core radius of the β model r_c , $r_s = r_c/0.22$ (Makino et al. 1998). Then, we calculated M_E in the same manner and obtained $M_{E, \text{NFW}} = 1.1^{+1.2}_{-0.5} \times 10^{12} M_{\odot}$. The upper limit is higher than the mass derived from the β model. However, the mass discrepancy cannot be explained even if only the NFW density profile is adopted. Therefore, we conclude that $M_{E, \text{NFW}} = 1.1^{+1.2}_{-0.5} \times 10^{12} M_{\odot}$ is a secure limit of the mass related to the main cluster, and it can explain 21 – 76% of M_{tot} as long as we estimate one-component gravitational potential. Note that, there is a possibility that the gravitational potential of the central lens galaxy was not measured properly since we used a single- β model. To evaluate the influence

Table 7. The result of the calculation of M_E . d_{EoH} means projected distance between each cluster center position determined by X-ray image fitting and the lens galaxy of the *Eye of Horus*

source	Main cluster	NE cluster
d_{EoH} (arcsec)	3.8	102
M_E (M_{\odot})	$1.1^{+0.7}_{-0.4} \times 10^{12}$	$6.1^{+1.4}_{-0.9} \times 10^{10}$

of the central lens galaxy, we tested to fit the X-ray surface brightness of the main cluster with a double- β model. Then we calculated M_E by stacking the components of the inner and the outer in the density ratio. However, we could not determine the mass since the normalization of the inner component has a large error ($M_E, 2\beta = 3.3^{+14.4}_{-2.4} \times 10^{12} M_{\odot}$). We did not consider the radial dependence of the temperature for the main cluster, but the Einstein ring is much smaller than the core radius of the main cluster ($25.0''$), and is located completely within it. And the ICM of the main cluster is well represented by a one-temperature model. Therefore, the influence of the radial dependence of the temperature is expected to be small.

Several studies reported that the hydrostatic mass is underestimated compared to M_{tot} derived from the strong lens data. Ota et al. (2004) reported that the hydrostatic mass of the strong lens cluster CL 0024+17 is smaller by a factor of 2–3. They discussed possibilities that there are additional mass components since the lens cluster is a line of sight merger, or that there are substructures in the central region of the lens cluster, and the mass profile follows the NFW density profile rather than the β model. Fig. 3 indicates that the main cluster has complex galaxy distribution along the line of sight of the *Eye of Horus*. There might be complex mass structures which are not considered in our analysis. To evaluate the degree of anisotropy of the mass distribution, we divided the area into the sectors of an opening angle of 90° in the NE, NW, SW and SE quadrants, and fitted the surface brightness distribution of each sector with a single- β model. However, since there are not enough photon counts, we could not find any significant difference in each parameter. Hashimoto-dani (1999) systematically studied 50 strong lens clusters and classified them into two types, one has the X-ray peak and the strong lens galaxy at the same center position, and the other at the different positions. He reported that the former and the latter follow $M_{\text{tot}}/M_E = 2.17 \pm 0.13$ and $M_{\text{tot}}/M_E = 3.33 \pm 0.39$, respectively. Since the X-ray peak of the main cluster is slightly shifted from the center of the lens galaxy, the *Eye of Horus* may follow the latter.

On the other hand, M_E of the NE cluster is only $\sim 2\%$ of the M_{tot} . This is probably because the gravitational potential of the NE cluster is concentrated in the central elliptical galaxy. Note that, however, several studies reported that the mass of the cluster whose center position is located far from the lens galaxy could affect the shape of lens image as external shear (e.g., Grillo et al. 2008). This effect needs to be considered in the detailed lens modeling of the *Eye of Horus* in future studies.

6 CONCLUSIONS

We observed X-ray emission around the *Eye of Horus* with *XMM-Newton* to evaluate the influence of cluster-scale mass structure on the lens image of the *Eye of Horus*. There are two clusters, the main cluster and the NE cluster which is located $\sim 100''$ northeast of the lens galaxy, and we found that the center position of the main cluster is located $3.8 \pm 1.0''$ south of the lens galaxy. The surface brightness distribution of the main cluster and the NE cluster is represented by a single, and a double β model, respectively. We also revealed that the spectrum of the main cluster is represented by a one-temperature model, while that of the NE cluster needs a two-temperature model.

The total mass projected on the sky plane within the Einstein radius M_{tot} determined by the Einstein radius is $\sim 3.0 \times 10^{12} M_{\odot}$, which is ~ 4.5 times larger than the stellar mass of the lens galaxy. We calculated the hydrostatic mass projected on the sky plane within the Einstein radius of the lens galaxy, M_{E} , using the X-ray data. M_{E} of the NE cluster is $6.1^{+1.4}_{-0.9} \times 10^{10} M_{\odot}$, which is only $\sim 2\%$ of M_{tot} . Therefore, the influence on M_{tot} is small. On the other hand, M_{E} of the main cluster is $1.1^{+0.7}_{-0.4} \times 10^{12} M_{\odot}$, which explains only 25–60% of M_{tot} . We tested an NFW density profile instead of the β model, and we obtained $M_{\text{E, NFW}} = 1.1^{+1.2}_{-0.5} \times 10^{12} M_{\odot}$, which can explain 21–76% of M_{tot} . Note that, the center position of the main cluster has a significant offset from the *Eye of Horus*, and the galaxy distribution suggests that the *Eye of Horus* has complex mass structures along the line of sight. There might be substructures along the line of sight, which are not considered in this work.

This is the first X-ray follow-up observation of the strong lens system discovered by Subaru-HSC, and we are planning to observe other strong lens systems with *XMM-Newton* and *Chandra*. Detailed modeling of the lensing of the *Eye of Horus* will be done, taking into account the result of this paper. When these observation and modeling are completed, we will be able to obtain robust constraint of the cosmological parameters and the gravitational structure of the distant galaxy.

ACKNOWLEDGEMENTS

The Hyper Suprime-Cam (HSC) collaboration includes the astronomical communities of Japan and Taiwan, and Princeton University. The HSC instrumentation and software were developed by the National Astronomical Observatory of Japan (NAOJ), the Kavli Institute for the Physics and Mathematics of the Universe (Kavli IPMU), the University of Tokyo, the High Energy Accelerator Research Organization (KEK), the Academia Sinica Institute for Astronomy and Astrophysics in Taiwan (ASIAA), and Princeton University. Funding was contributed by the FIRST program from Japanese Cabinet Office, the Ministry of Education, Culture, Sports, Science and Technology (MEXT), the Japan Society for the Promotion of Science (JSPS), Japan Science and Technology Agency (JST), the Toray Science Foundation, NAOJ, Kavli IPMU, KEK, ASIAA, and Princeton University.

This paper makes use of software developed for the Large Synoptic Survey Telescope. We thank the LSST

Project for making their code available as free software at <http://dm.lsst.org>

The Pan-STARRS1 Surveys (PS1) have been made possible through contributions of the Institute for Astronomy, the University of Hawaii, the Pan-STARRS Project Office, the Max-Planck Society and its participating institutes, the Max Planck Institute for Astronomy, Heidelberg and the Max Planck Institute for Extraterrestrial Physics, Garching, The Johns Hopkins University, Durham University, the University of Edinburgh, Queen's University Belfast, the Harvard-Smithsonian Center for Astrophysics, the Las Cumbres Observatory Global Telescope Network Incorporated, the National Central University of Taiwan, the Space Telescope Science Institute, the National Aeronautics and Space Administration under Grant No. NNX08AR22G issued through the Planetary Science Division of the NASA Science Mission Directorate, the National Science Foundation under Grant No. AST-1238877, the University of Maryland, and Eotvos Lorand University (ELTE) and the Los Alamos National Laboratory.

This work is supported in part by the Ministry of Science and Technology of Taiwan (grant MOST 106-2628-M-001-003-MY3) and by Academia Sinica (grant AS-IA-107-M01).

This work is also supported in part by World Premier International Research Center Initiative (WPI Initiative), MEXT, Japan, and JSPS KAKENHI Grants Number JP15H05892, JP17H02868, JP18K03693 and JP19H05189.

K.C.W. is supported in part by an EACOA Fellowship awarded by the East Asia Core Observatories Association, which consists of the Academia Sinica Institute of Astronomy and Astrophysics, the National Astronomical Observatory of Japan, the National Astronomical Observatories of the Chinese Academy of Sciences, and the Korea Astronomy and Space Science Institute.

REFERENCES

- Aihara H., et al., 2018a, *PASJ*, **70**, S4
 Aihara H., et al., 2018b, *PASJ*, **70**, S8
 Arnaud K. A., 1996, in Jacoby G. H., Barnes J., eds, *Astronomical Society of the Pacific Conference Series Vol. 101, Astronomical Data Analysis Software and Systems V*. p. 17
 Bosch J., et al., 2018, *PASJ*, **70**, S5
 Carter J. A., Sembay S., 2008, *A&A*, **489**, 837
 Cash W., 1979, *ApJ*, **228**, 939
 Collett T. E., Auger M. W., 2014, *MNRAS*, **443**, 969
 Collett T. E., Auger M. W., Belokurov V., Marshall P. J., Hall A. C., 2012, *MNRAS*, **424**, 2864
 Coupon J., Czakov N., Bosch J., Komiyama Y., Medezinski E., Miyazaki S., Oguri M., 2018, *PASJ*, **70**, S7
 De Luca A., Molendi S., 2004, *A&A*, **419**, 837
 Freeman P., Doe S., Siemiginowska A., 2001, in Starck J.-L., Murtagh F. D., eds, *Proc. SPIE Vol. 4477, Astronomical Data Analysis*. pp 76–87 ([arXiv:astro-ph/0108426](https://arxiv.org/abs/astro-ph/0108426)), [doi:10.1117/12.447161](https://doi.org/10.1117/12.447161)
 Freyberg M. J., et al., 2004, in Flanagan K. A., Siegmund O. H. W., eds, *Proc. SPIE Vol. 5165, X-Ray and Gamma-Ray Instrumentation for Astronomy XIII*. pp 112–122, [doi:10.1117/12.506277](https://doi.org/10.1117/12.506277)
 Fruscione A., et al., 2006, in *Society of Photo-Optical Instrumentation Engineers (SPIE) Conference Series*. p. 62701V, [doi:10.1117/12.671760](https://doi.org/10.1117/12.671760)

- Fujita Y., Koyama K., Tsuru T., Matsumoto H., 1996, *PASJ*, **48**, 191
- Furusawa H., et al., 2018, *PASJ*, **70**, S3
- Grillo C., et al., 2008, *A&A*, **486**, 45
- Hashimotodani K., 1999, PhD dissertation, Osaka Univ.
- Huang S., et al., 2018, *PASJ*, **70**, S6
- Kalberla P. M. W., Burton W. B., Hartmann D., Arnal E. M., Bajaja E., Morras R., Pöppel W. G. L., 2005, *A&A*, **440**, 775
- Kawanomoto S., et al., 2018, *PASJ*, **70**, 66
- Keeton C. R., Zabludoff A. I., 2004, *ApJ*, **612**, 660
- Komatsu E., et al., 2011, *ApJS*, **192**, 18
- Komiyama Y., et al., 2018, *PASJ*, **70**, S2
- Kuntz K. D., Snowden S. L., 2008, *A&A*, **478**, 575
- Linder E. V., 2016, *Phys. Rev. D*, **94**, 083510
- Lodders K., Palme H., 2009, *Meteoritics and Planetary Science Supplement*, **72**, 5154
- Makino N., Sasaki S., Suto Y., 1998, *ApJ*, **497**, 555
- Miyaoka K., et al., 2018, *PASJ*, **70**, S22
- Miyazaki S., et al., 2018, *PASJ*, **70**, S1
- Navarro J. F., Frenk C. S., White S. D. M., 1996, *ApJ*, **462**, 563
- Oguri M., et al., 2018, *PASJ*, **70**, S20
- Okabe N., et al., 2018, arXiv e-prints,
- Ota N., Mitsuda K., 2004, *A&A*, **428**, 757
- Ota N., Mitsuda K., Fukazawa Y., 1998, *ApJ*, **495**, 170
- Ota N., Pointecouteau E., Hattori M., Mitsuda K., 2004, *ApJ*, **601**, 120
- Smith R. K., Brickhouse N. S., Liedahl D. A., Raymond J. C., 2001, *ApJ*, **556**, L91
- Snowden S. L., Collier M. R., Kuntz K. D., 2004, *ApJ*, **610**, 1182
- Snowden S. L., Mushotzky R. F., Kuntz K. D., Davis D. S., 2008, *A&A*, **478**, 615
- Sonnenfeld A., Treu T., Gavazzi R., Marshall P. J., Auger M. W., Suyu S. H., Koopmans L. V. E., Bolton A. S., 2012, *ApJ*, **752**, 163
- Sonnenfeld A., Jaelani A. T., Chan J. H. H., More A., Suyu S. H., Wong K. C., Oguri M., Lee C.-H., 2019, arXiv e-prints,
- Strüder L., et al., 2001, *A&A*, **365**, L18
- Tanaka M., 2015, *ApJ*, **801**, 20
- Tanaka M., et al., 2016, *ApJ*, **826**, L19
- Turner M. J. L., et al., 2001, *A&A*, **365**, L27

This paper has been typeset from a $\text{\TeX}/\text{\LaTeX}$ file prepared by the author.